BIOPHYSICS

MINFLUX dissects the unimpeded walking of kinesin-1

Jan O. Wolff[1]†, Lukas Scheiderer[1]†, Tobias Engelhardt[1]‡, Johann Engelhardt[1], Jessica Matthias[1]‡, Stefan W. Hell[1,2]*

We introduce an interferometric MINFLUX microscope that records protein movements with up to 1.7 nanometer per millisecond spatiotemporal precision. Such precision has previously required attaching disproportionately large beads to the protein, but MINFLUX requires the detection of only about 20 photons from an approximately 1-nanometer-sized fluorophore. Therefore, we were able to study the stepping of the motor protein kinesin-1 on microtubules at up to physiological adenosine-5′-triphosphate (ATP) concentrations. We uncovered rotations of the stalk and the heads of load-free kinesin during stepping and showed that ATP is taken up with a single head bound to the microtubule and that ATP hydrolysis occurs when both heads are bound. Our results show that MINFLUX quantifies (sub)millisecond conformational changes of proteins with minimal disturbance.

Exploring movements and conformational changes of proteins lies at the heart of unraveling the inner workings of a cell, but the tools for accomplishing this task have so far been limited. Nanometer-sized protein motions of millisecond duration can be retrieved by tethering the protein to a bead held in an infrared optical trap and measuring the bead's movement (*1*–*3*). However, this preparation subjects the protein to a force and thus does not allow the direct observation of its entirely free motion. The 70- to 500-nm-diameter beads required for optical trapping are also orders of magnitude larger than the protein itself, which also causes problems, including susceptibility to laser-induced heating (*4*). Alternatively, a protein can be observed with no or minimal restrictions by labeling it with an ~1-nm-sized organic fluorophore and recording its motion with the camera of a light microscope (*5*, *6*). The position of the label is then inferred from the peak of the fluorescence diffraction pattern rendered by N camera-detected photons. Unfortunately, the resulting localization precision σ scales with $1/\sqrt{N}$, meaning that σ = 1 to 2 nm typically requires $N > 2500$ photons (*7*). Thus, even the brightest fluorophores entail localization times of hundreds of milliseconds. Fluorescence-based localization therefore cannot live up to the spatiotemporal resolution (STR) provided by optical traps. Replacing the tiny fluorophore with a laser-scattering gold bead of ≥30 nm diameter (*8*–*10*) can compensate for this shortfall, but the volume, drag, and electrostatic interactions of the gold bead preclude unimpeded protein motion.

These limits are also reflected in the understanding of the arguably best-studied moving protein, the homodimeric motor protein kinesin-1, hereafter called kinesin, which is responsible for the anterograde transport on microtubules and the malfunction of which is linked to diseases (*11*–*14*). Although the above tools have greatly advanced our understanding of how kinesin walks, many details of its mechanochemical cycle have remained controversial or elusive (*15*, *16*).

We reasoned that MINFLUX (*17*), a recently introduced microscopy method for localizing fluorophores with a minimal rather than a maximal number of detected photons N, should greatly improve the study of protein movements. For a given N, MINFLUX (*17*–*20*) typically renders an STR of $\sigma\sqrt{\tau}$ with ~10-fold improved σ, or a 100-fold increased temporal resolution τ compared with popular camera-based localizations (*18*). Using a single fluorophore of ~1 nm in size, an STR is attained that has so far required the use of bulky beads. This combination of STR and a small label has motivated us to revisit the walking of kinesin. Here, we report on an interferometric MINFLUX implementation that delivers nanometer/submillisecond STR in protein tracking. Harnessing this STR, we determined the steps and substeps of the heads and the stalk of kinesin. The direct observation of unhindered substeps allowed us to determine in which state adenosine-5′-triphosphate (ATP) binds and hydrolyzes and to uncover orientation changes of functional subunits of kinesin during stepping. Our study concomitantly establishes MINFLUX as a tool for examining fast protein movements and conformational changes at nanometer scale with minimal or no impediment.

Interferometric MINFLUX maximizes fluorophore localization precision

A scanning MINFLUX microscope features a beam for fluorophore excitation with a central intensity minimum ("zero") that is positioned in the sample with subnanometer precision. Emitted photons are counted by a confocal point detector (Fig. 1A). The closer the central excitation minimum is to the fluorophore, the lower the fluorescence rate, meaning that the number of detections readily discloses the distance between the unknown position of the fluorophore and the perfectly known position of the minimum. In fact, the intensity of the excitation beam around the minimum increases quadratically with distance to the minimum (Fig. 1B), with steepness depending on the beam's focusing angle, wavelength, and power. Therefore, the fluorescence detection rate displays the same quadratic dependence on the fluorophore-to-minimum distance (Fig. 1B). If the rate is minimal, i.e., down to background level, then the fluorophore is localized because the position of the fluorophore coincides with that of the excitation beam minimum. However, because of the adverse role of background, matching the two positions at the angstrom level is usually not possible. Fortunately, such perfect matching is not needed because the mismatch and thus the fluorophore position can be precisely derived from a relatively small number of photons N gained by targeting the minimum to two or more positions within a small spatial interval L containing the fluorophore (Fig. 1B).

MINFLUX localization of a fluorophore located at an unknown position within the diffraction limit (~200 nm) is performed iteratively (*19*) by continually shifting the minimum closer to the fluorophore. The localization usually starts out from an interval L of ~200 nm, which is then reduced on the basis of the initially derived precision σ_0. In theory, an iterative reduction of L in proportion to the precision σ_{k-1} of the previous step, $L_k = \alpha\sigma_{k-1}$, gives rise to an exponential increase in precision after k steps: $\sigma_k = \sigma_0 \exp\left(-\frac{8N}{e\alpha^2}\right)$. The parameter α ensures that the next L_k is small enough to quickly zoom in on the fluorophore but large enough to keep the fluorophore within the next interval. This exponential increase in precision with N signifies a most efficient use of the detected photons and should be contrasted with the sluggish $1/\sqrt{N}$ dependence in camera-based localization (see supplementary text section 2.2). The reduction of L_k ends just before the quadratic dependence disappears amid background. Therefore, practical MINFLUX localization precision σ is limited by the steepness-to-background ratio of the excitation beam. In principle, steepness can be arbitrarily increased by increasing the beam power, but because this measure also increases the background, we designed a MINFLUX system that inherently yields higher steepness compared with reported donut-based systems (*17*–*20*).

[1]Department of Optical Nanoscopy, Max Planck Institute for Medical Research, Heidelberg, Germany. [2]Department of NanoBiophotonics, Max Planck Institute for Multidisciplinary Sciences, Göttingen, Germany.
*Corresponding author. Email: shell@gwdg.de
†These authors contributed equally to this work.
‡Present address: Abberior Instruments GmbH, Göttingen, Germany.

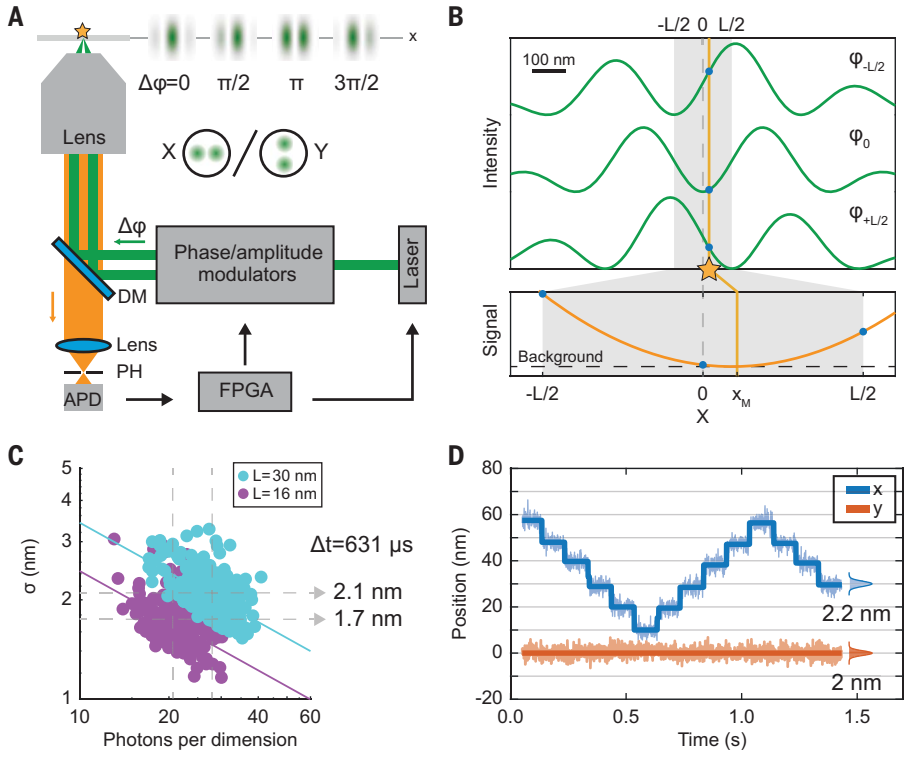

Fig. 1. Interferometric MINFLUX microscope provides nanometer localization precision of a fluorophore with 20 to 40 detected photons. (**A**) Simplified setup. A 640-nm laser beam is shaped by a phase modulator and an amplitude modulator to create a pair of beams with a defined phase difference φ in the entrance pupil of an objective lens. Their interference creates an intensity pattern with a local line-shaped minimum in the focal plane. The minimum is shifted by changing φ with the phase/amplitude modulator. Two orthogonal pairs of beams are used for covering both the x and y directions. The fluorescence collected by the lens passes a dichroic mirror (DM) that otherwise deflects the laser light, is focused onto a confocal pinhole (PH), and is detected by an avalanche photodiode (APD). The (x,y) localization algorithm is implemented in a field programmable gate array (FPGA) directing the minimum to specified (x,y) positions, depending on the number of photons detected by the APD. (**B**) Top: MINFLUX localization in one dimension, using a change of φ to place the minimum at positions −L/2, 0, and L/2 of a linear interval around the expected molecule position x_M. Bottom: The photons counts measured with the minimum at these three points allow retrieving x_M by fitting with a parabola. In iterative MINFLUX localizations in which the excitation intensity minimum approaches the fluorophore, the laser power is increased accordingly to keep the fluorescence rate at the same level. Background is caused by nonvanishing excitation intensity at the minimum, stray light, and detector dark counts. (**C**) Localization precision σ of single surface–immobilized ATTO 647N fluorophores using L = 30 nm (263 fluorophores) and L = 16 nm (232 fluorophores), yielding σ = 2.1 and 1.7 nm, respectively. (**D**) Tracking of a single fluorophore moved by a piezoelectric stage [L = 30 nm, 2 nm residual noise, 0.607 ms temporal resolution, 70 photons per (x,y) localization] with corresponding step fit in the x direction and constant fit in the y direction.

Specifically, our MINFLUX setup featured two pairs of oblique beams that interfered destructively in the focal plane (Fig. 1A). One of the pairs was arranged in the x direction, rendering a y-oriented line-shaped minimum for x localization; the pair for y localization was arranged accordingly in the y direction. Line-shaped minima have also been used in stimulated emission depletion (STED) microscopy (*21*) because they require fewer polarization and aberration optimizations while providing higher steepness (fig. S1) and lower background. Altering the phase difference of the x-arranged beams moved the y-oriented line-shaped minimum with angstrom precision in the x direction and vice versa. By targeting the minima to coordinates $-L_k/2$, 0 and $L_k/2$ around the last estimated fluorophore position, the position was iteratively established for each dimension (x and y) on the basis of the number of detections (Fig. 1B). The (x,y) trajectory was obtained by repeatedly switching between x and y using an electro-optical modulator (figs. S2 and S3). Once L_k =16 nm was reached, as few as ~20 detected photons sufficed to localize single immobilized ATTO 647N fluorophores with an average precision σ = 1.7 nm per dimension (Fig. 1C). For L_k = 30 nm, a precision σ = 2.1 nm was obtained with ~28 photons. Because the average signal-to-background ratio was more than three times higher for L_k = 30 nm, we performed all tracking measurements with L_k= L = 30 nm (fig. S4), ensuring robustness in the process. In fluorophore tracking, the successive small changes in fluorophore position inherently allow for the continual use of L = 30 nm and thus for the maximal use of the N photons detected.

The tracking accuracy of our MINFLUX system was highlighted by moving an individual ATTO 647N fluorophore on a periodic stepping trajectory along the x axis of a piezoelectric stage (Fig. 1D). The steps were fitted with an algorithm based on an iterative change-point search (*22*) that was used throughout our study. Our analysis showed that ~70 photons recorded within 607 µs clearly identified the steps with σ = 2 nm in both the x and y directions.

MINFLUX observes substeps and stalk rotation of kinesin

Under consumption of an ATP molecule, the catalytic motor domains (heads) of kinesin take hand-over-hand steps of 16 nm (regular steps), amounting to twice the tubulin dimer spacing. Their conjoining coiled-coil stalk domain is thus translocated in discrete 8-nm steps (*1*, *3*, *6*, *23*). However, it is still debated (*24*–*26*) whether kinesin walks "like a human," i.e., with one head passing the stalk on the left and the other one on the right (asymmetric), or if it walks with both heads passing on the same side (symmetric). Camera localization–based fluorescence imaging with one-nanometer accuracy (FIONA) (*5*) resolved regular kinesin steps using a single fluorophore label at one of the heads, but its time resolution of several hundreds of milliseconds required slowing down movement by administering ATP concentrations that were ~1000 times lower than in a cell (*6*). In fact, addressing steps at physiological ATP concentrations has so far required the use of beads that are orders of magnitude larger than the kinesin heads.

For example, an optical trap study recently observed force-dependent substeps by tracking a germanium bead of ~70 nm diameter attached to the kinesin stalk (*27*). Thus, as in all optical trap experiments, only the movements of the protein center of mass could be examined, not those of the individual heads. Although a ≥30-nm gold bead bound to a kinesin head allowed tracking the heads, different studies came to opposing results regarding the long-standing question of when ATP is bound (*15*, *16*). In fact, simulations (*28*, *29*) suggested that this discrepancy is caused by the different labeling positions because the beads are >200 times larger in volume than the kinesin head.

Harnessing MINFLUX, we investigated the stepping of different cysteine-light, truncated,

and cargo-free kinesin constructs labeled with a fluorophore at various protein positions through maleimide coupling. The kinesin molecules were introduced into a flow cell in which biotinylated and fluorescently labeled (Alexa Fluor 488) microtubules were attached through neutravidin to a PLL-PEG-biotin polymer–coated coverslip. For kinesin center-of-mass tracking, we labeled construct N356C at its solvent-exposed cysteine introduced into the stalk (Fig. 2A).

We recorded one-dimensional (1D) traces of individual kinesin dimers labeled with a single fluorophore (degree of labeling of 1, DOL1) on the stalk walking along the microtubule axis (on-axis displacement) with a temporal resolution of ~1 ms and a precision of $\sigma \approx 1.7$ nm (Fig. 2, B and C). These initial measurements were performed at a 10 μM ATP concentration, providing a walking speed of ~280 nm/s. The traces were recorded with run lengths up to ~180 nm. On the basis of the residual noise and the number of localizations between steps, we determined a median precision of the measured step size of 0.57 nm (Fig. 2D). A histogram of all kinesin center-of-mass steps revealed a size range of ~3 to 11 nm (Fig. 2E), with equally high peaks centered at 8 and 4 nm, corresponding to expected regular steps and substeps, respectively. The latter have so far not been observed without attaching a much bigger bead to the protein (*27*).

With the same kinesin construct, we also recorded traces at a physiological 1 mM ATP concentration. Despite the now increased walking speed of ~550 nm/s, both regular steps and substeps of the kinesin center of mass were resolved (fig. S5). The substantially smaller fraction of detected substeps indicated a reduced detection efficiency caused by the shorter substep dwell times (fig. S6). The step-size histogram did not exhibit its maximum at 8 nm, as would be expected for regular center-of-mass steps, but rather showed an unexpectedly high occurrence of 6- and 10-nm steps (Fig. 3A, middle). Plotting the sequence of consecutive step sizes in a 2D histogram revealed that their sum frequently matched 16 nm, indicating that these unusual steps typically occurred sequentially (Fig. 3A, right). The nonzero radius of the stalk (~1.0 nm, inferred from PDB 1D7M) and the distance between the maleimide and the fluorophore (up to ~1.0 nm; fig. S7) added up to a total fluorophore displacement of up to ~2 nm from the stalk axis of kinesin. Therefore, assuming that the fluorophore displacement vector had a component parallel to the walking direction, we reasoned that the observed stepping asymmetry was caused by a rotation of the stalk during a regular step (Fig. 3A, left).

To test this hypothesis, we labeled the same construct with an excess of fluorophores, ensuring that the cysteines at amino acid position 356 (aa356) of both monomers each carried a fluorophore (degree of labeling of 2, DOL2) (figs. S7 and S8). As a result, we found stepping symmetry reinstated, because MINFLUX inherently localized the midpoint between two adjacent identical fluorophores, which by design coincided with the stalk axis (Fig. 3B, left). To ensure that the histogram of the DOL2 experiment exclusively represents steps of kinesins with both fluorophores emitting, only DOL2 tracking data (characterized by a photon rate >167 kHz, as determined from the DOL1 data; fig. S9) were plotted. Supporting our hypothesis of a stalk rotation, the resulting step-size histogram indeed shows a rather narrow peak centered at 8 nm (Fig. 3B, middle), and the 2D histogram of consecutive step sizes indicates the dominance of successive 8-nm steps (Fig. 3B, right). In a trace (fig. S10) in which one of the fluorophores bleached, a clear difference in the step sizes before and after bleaching became apparent: ~8 nm (before) and alternating ~10 and 6 nm (after). We conclude that the stalk rotates when kinesin steps. Whether consecutive steps cause a unidirectional (*26*, *30*) or a back-and-forth (*24*, *25*) rotation cannot be deduced from this experiment alone.

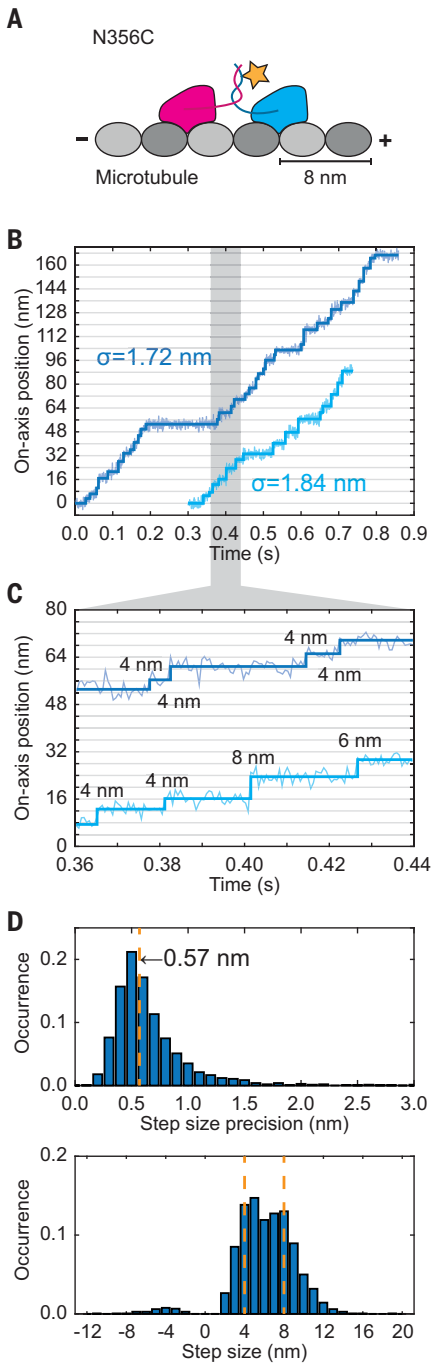

Fig. 2. MINFLUX tracking of kinesin exhibits 4-nm center-of-mass substeps. (**A**) Scheme of kinesin walking on a microtubule indicating the labeling position of the fluorophore in the stalk. (**B**) Exemplary position traces recorded along the microtubule axis at 10 μM ATP. The data are overlaid with the detected step function shown as thick darker lines. (**C**) Magnification of the traces shown in (B) between 0.36 and 0.44 s as highlighted by gray shading. (**D**) Histograms of the step-size precision (top) and the step sizes (bottom) for 1821 steps. The median step-size precision is 0.57 nm. Orange dashed lines highlight 4-nm-sized substeps and 8-nm-sized regular steps.

ATP binds in one-head-bound state

Next, we explored whether ATP binds to kinesin in its one-head-bound state (1HB, only leading head bound) or its two-head-bound state (2HB, leading and trailing head associated with their binding site), a longstanding open question concerning the kinesin mechanochemical cycle (*15*, *16*, *31*–*35*). We used construct T324C labeled at its solvent-exposed cysteine (DOL1) located at the C-terminal end of the α6 helix adjacent to the neck linker on the head. When the head is microtubule bound, the label is in the center on the right side of the motor domain with respect to the walking direction and the microtubule surface is beneath the head. We recorded 2D traces along (on-axis) and perpendicular to (off-axis) the microtubule axis at ATP concentrations of 10 μM, 100 μM, and 1 mM. By tracking one of the heads rather than the kinesin center of mass, we observed traces with regular steps of 16 nm, the distance between every second binding site on the microtubule, and substeps of ~8 nm resulting from the labeled head occupying an unbound intermediate state (Fig. 4A). Accordingly, the on-axis step-size histogram shows a fraction of regular steps peaking at 16 nm and a fraction of substeps distributed at ~8 nm. In good agreement with the results obtained from construct N356C, the fraction of detected substeps decreased with increasing ATP concentration, indicating an ATP dependence of the unbound state (Fig. 4B). Note the unexpectedly broad distribution of substep sizes for T324C, which is discussed below.

To explicitly identify the bound states (B), in which the labeled kinesin head is located at its microtubule-binding site, and unbound states (U), in which it is located in between, we applied a hidden Markov model (HMM) based solely on the existence of ~8-nm substeps and the possibility of kinesin detaching and reattaching to the microtubule. The model identifies five different state transitions from the sequence of detected steps (see materials and methods section 1.4.7). All substeps correspond to the labeled head transitioning between the two states (B→U and U→B). However, when they are unpaired, related to a rare and not directly observable "slip state," the head effectively transitions between bound states (B→B, see next section). Transitions between microtubule-binding sites (B→B), during which the intermediate unbound state was too short and thus missed, were identified as the most likely source of the ~16-nm steps. Potential ~16-nm transitions between unbound states (U→U) of the labeled head comprise a series of the transitions explained above (labeled head U→B, unlabeled head B→U and U→B, and labeled head B→U), so missing these states was deemed as highly unlikely (see supplementary text section 2.4).

On the basis of these premises, we assigned bound and unbound states to all traces of the kinesin construct T324C with the HMM (see representative trace in Fig. 4C). Using this assignment, the dwell times in the bound and unbound states were determined for each ATP concentration. To obtain the average dwell times τ_{1HB} and τ_{2HB} of the underlying 1HB and 2HB states, respectively, the histograms of residence time in the bound and unbound states were fitted simultaneously (fig. S11). The unbound state (1HB with labeled head unbound) data were fitted with a monoexponential decay function. For the bound state (2HB with labeled head leading, 1HB with labeled head bound, and 2HB with labeled head trailing), a combination of three exponential decay functions was used under the assumption of equal binding kinetics for both heads. Matching the trend deduced from the step-size histograms in Fig. 4B, τ_{1HB} substantially increased with decreasing ATP concentrations from ~8 ms for 1 mM ATP to >30 ms for 10 μM ATP (Fig. 4D). By contrast, τ_{2HB} did not exhibit any ATP dependence, displaying a dwell time of ~8 ms for all ATP concentrations. We concluded that ATP binds [presumably to the microtubule-bound leading head (*31*)] when kinesin is in its 1HB state and the unbound head is in between previous and next microtubule-binding sites.

ATP hydrolyzes in the 2HB state

Subsequently, we recorded traces of the kinesin construct T324C with 1 mM ATPγS, a slowly hydrolyzing ATP analog. The results revealed that the use of ATPγS did not really

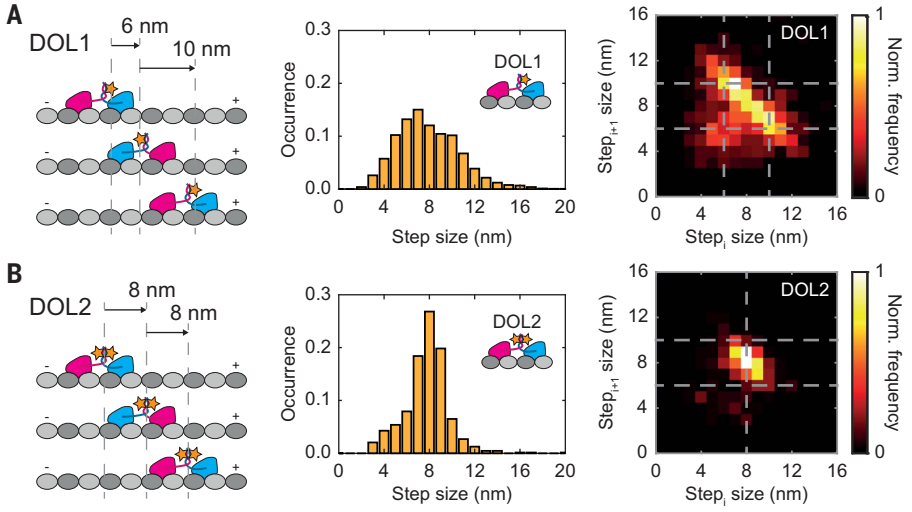

Fig. 3. Rotation of the stalk during kinesin stepping. (**A**) Left: Suggested model of stalk rotation explaining the alternating sequence of larger and smaller steps at DOL1. Middle: Step-size histogram for 1D kinesin center-of-mass tracking with a single fluorophore (DOL1, Number of steps S_{DOL1} = 1810) at 1 mM ATP concentration. Right: 2D histogram of consecutive step sizes showing alternating 6- and 10-nm steps for DOL1. (**B**) Left: Suggested model of stalk rotation demonstrating the true 8-nm stalk displacement at DOL2. Middle: Step-size histogram for 1D kinesin center-of-mass tracking with two fluorophores on both protein-labeling sites of the kinesin dimer (DOL2, S_{DOL2} = 630) at 1 mM ATP concentration. Right: 2D histogram of consecutive step sizes showing predominantly successive 8-nm steps for DOL2.

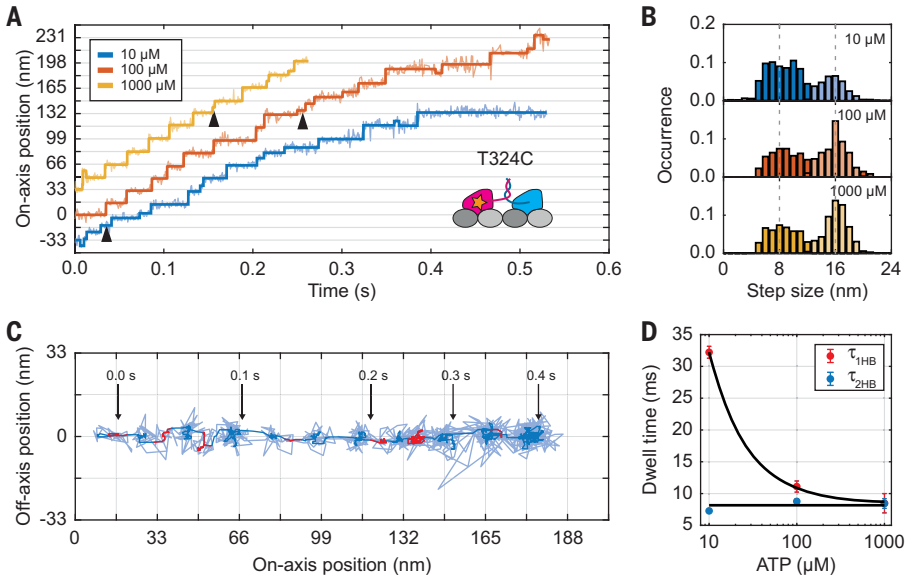

Fig. 4. Kinesin awaits ATP binding in 1HB state. (**A**) Exemplary traces recorded at 10 μM (blue), 100 μM (orange), and 1 mM (yellow) ATP concentrations with distinct plateaus spaced by ~16 nm. Exemplary substep plateaus between two 8-nm steps are highlighted by black arrowheads. The inlay shows construct T324C with the fluorophore at the labeling position on one kinesin head. (**B**) Histogram of detected step sizes for each ATP concentration showing ~8-nm substeps (darker filling; $S_{10\mu M}$ = 1152, $S_{100\mu M}$ = 230, and S_{1mM} = 905) and 16-nm regular steps (lighter filling; $S_{10\mu M}$ = 557, $S_{100\mu M}$ = 254, and S_{1mM} = 1110) as assigned by the HMM. (**C**) 2D representation of the 10 μM trace shown in (A) with time stamps. Plateaus identified by the HMM as unbound states are highlighted in red. For improved visibility, the raw data points are overlaid with a 5-ms moving median filter. (**D**) Comparison of τ_{1HB} and τ_{2HB} for different ATP concentrations. Black lines show the fitted Michaelis-Menten kinetics (K_m = 28 ± 2 μM, k_{ATP} = 4.2 ± 0.4 s^{-1} μM^{-1}) for the 1HB state and a constant fit (τ_{2HB} = 8.5 ms) for the 2HB state. Error bars and parameter uncertainties denote the 64% confidence intervals of the fits.

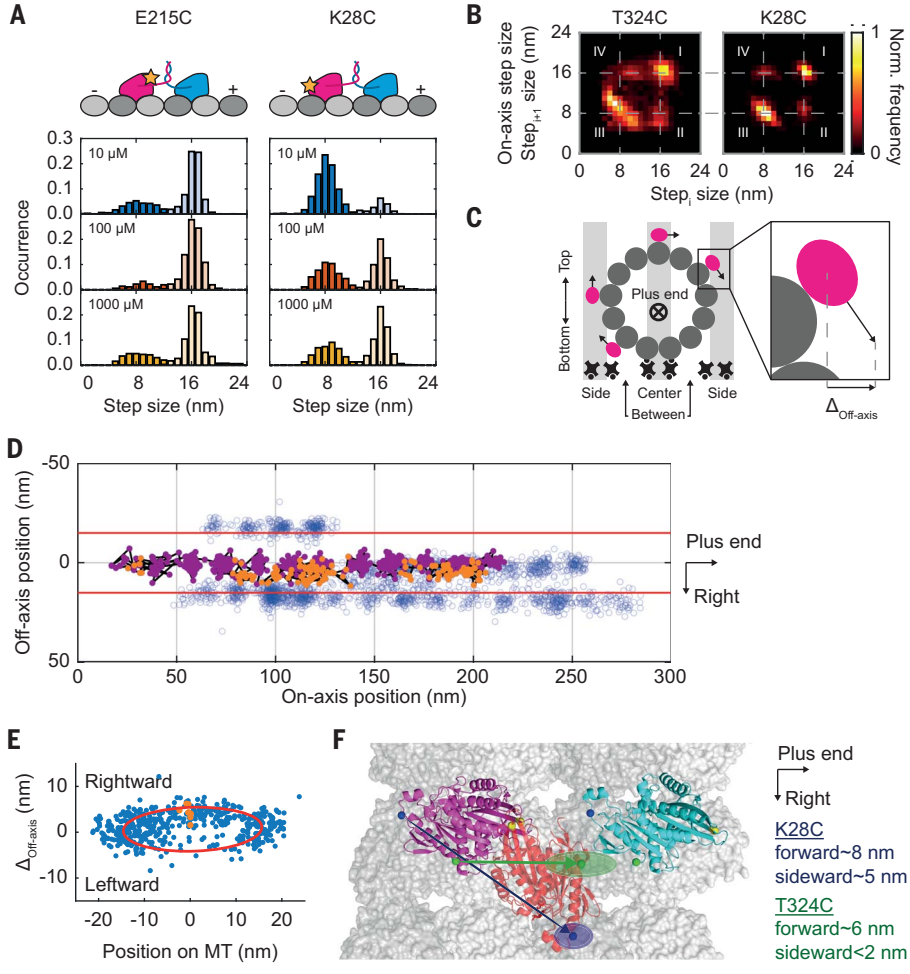

Fig. 5. Rotation of the unbound head reconstructed by tracking various labeling sites on the kinesin head. (**A**) Left: Construct E215C with the fluorophore-labeling site on the front end of the kinesin head and histograms of the detected step sizes of this construct for 10 μM, 100 μM, and 1 mM ATP concentrations, respectively, featuring a dominant peak at 16 nm ($S_{10\mu M}$ = 666, $S_{100\mu M}$ = 310, and S_{1mM} = 431) and a small fraction of ~8-nm steps ($S_{10\mu M}$ = 280, $S_{100\mu M}$ = 50, and S_{1mM} = 195). Right: Construct K28C with labeling position at the back of the kinesin head and histograms of detected step sizes of this construct for 10 μM, 100 μM, and 1 mM ATP concentration, respectively, featuring an increasing peak at 16 nm ($S_{10\mu M}$ = 154, $S_{100\mu M}$ = 236, and S_{1mM} = 529) and a decreasing fraction of ~8-nm steps ($S_{10\mu M}$ = 718, $S_{100\mu M}$ = 217, and S_{1mM} = 361) for increasing ATP concentrations. (**B**) 2D histograms of consecutive step sizes for constructs T324C and K28C, both showing successive regular steps (I), regular steps followed by substeps (II), successive substeps (III), and substeps followed by regular steps (IV). For construct K28C, transitions involving the unbound state generate symmetric successive steps of ~8 nm. For construct T324C, these transitions exhibit an asymmetry of ~6-nm substeps followed by ~10-nm substeps. (**C**) Schematic of a surface-immobilized microtubule and the assignment of protofilament classes. The assumed true sideward displacement of the kinesin head (magenta) in these classes is indicated by black arrows. Magnification visualizes the projection of the 3D displacement onto the imaging plane. (**D**) Scatter plot of four kinesin traces recorded on a single microtubule (blue circles) with one central trace highlighted for the detected bound (dark magenta dots) and unbound (orange dots) states. Red lines display the microtubule outline inferred from the traces. (**E**) Sideward displacement of all detected unbound states and their respective position on the microtubule (blue dots). The orange dots correspond to the sideward displacement of the central trace shown in (E). The red line displays an ellipse fit to the data with a major axis diameter of 30.6 nm and a minor axis diameter of 9.2 nm. (**F**) Proposed 3D orientation of the unbound state of the trailing head (orange; PDB: 1MKJ) on the microtubule (alpha-tubulin is shown in dark gray, beta-tubulin in light gray, PDB: 6DPU). Colored arrows depict the displacement of the different labeling positions from the microtubule-bound state of the trailing head (dark magenta; PDB: 3J8Y). Uncertainties of the positions for aa28 and aa324 are displayed by the shaded regions representing the Gaussian width of the step-size distribution. The leading head is shown in the apo state (cyan; PDB: 4ATX).

affect the unbound state duration but did substantially increase the time spent in the bound state (fig. S11). Therefore, we conjectured that ATP hydrolysis did not take place in the 1HB state, but rather after the unbound head moved to its next binding site. This hypothesis was further supported by comparing the run length (actual distance traveled) and run fraction (ratio of run length and distance from starting point to end of microtubule) determined from kymographs of total internal reflection fluorescence (TIRF) microscopy measurements for construct T324C under ATPγS and under ATP consumption. For 1 mM ATPγS, kinesin walked 36 times more slowly but with an average run length nearly as long and an average run fraction nearly as large as for 1 mM ATP. (The observed slight reduction of run length was likely caused by increased bleaching over the much longer run time.) Whereas walking speeds were comparable for 1 mM ATPγS and 1 μM ATP, the run length was substantially shorter and the run fraction substantially smaller for 1 μM ATP (fig. S12). Because the 1HB state is known to be the one that is most vulnerable to kinesin detachment from the microtubule (*36*), the combined results disqualify 1HB as being the ATP-hydrolyzing state.

Further examination of the traces revealed a rare occurrence of an uneven number of ~8-nm-sized substeps between regular ~16-nm-sized steps (fig. S13) without concurrent side stepping. We reasoned that the lack of a second corresponding substep probably arose from kinesin detaching into a weakly bound slip state and subsequently reattaching to the microtubule before or after an unpaired substep. When the heads change binding positions on the microtubule, an uneven number of intermediate substeps is expected in the traces. Such a slip state has so far only been reported for kinesin under load (*27*, *37*), not for freely walking kinesin.

Reconstruction of unbound head orientation during stepping

To explore the 3D orientation of the unbound head, we repeated the 2D-MINFLUX tracking experiments with two additional kinesin constructs: E215C labeled at its solvent-exposed cysteine located at the C-terminal end of the β6-sheet (Fig. 5A, top left) and K28C labeled at its solvent-exposed cysteine at aa28 (Fig. 5A, top right). In the bound state, the labeling positions of E215C and K28C are located in the very front and back of the head, respectively, relative to the walking direction. The fraction of detected pairs of substeps (B→U and U→B) of construct E215C did not differ substantially for 10 μM, 100 μM, and 1 mM ATP. Unlike in

previous experiments with construct T324C (Fig. 4B), these fractions always amounted to only ~10% of the entire population of substep pairs and regular steps (Fig. 5A, bottom left). In fact, compared with construct T324C (especially for 10 μM ATP), this fraction was substantially smaller and the unbound state was substantially shorter (fig. S14). By contrast, construct K28C (Fig. 5A, right) did not notably differ in these aspects from construct T324C, indicating that the observed substeps of E215C do not represent the real 1HB state of the labeled head (for details, see supplementary text section 2.5). The substep peak of the step-size histogram of construct K28C was sharper than that of T324C, with a clear peak centered at 8 nm. Plotting the sequence of consecutive step sizes in 2D histograms revealed an asymmetry of 6-nm B→U substeps and subsequent 10-nm U→B substeps of construct T324C, which is in contrast to the symmetric substepping behavior of the K28C construct (Fig. 5B).

We cannot fully exclude that the modification at aa215 hampered kinesin from entering a detectable 1HB state caused by altered protein-protein interactions or steric hindrance. However, this scenario disagrees with earlier Förster resonance energy transfer (FRET)–based observations of the 1HB state of a kinesin construct that was point mutated and labeled at aa215 (*38*). Therefore, we advance the following reasoning. Because MINFLUX tracks the fluorophore position, our traces actually represent displacements of individual amino acids. Specifically, they map projections of the 3D amino acid trajectories onto the focal plane. Differences in substeps between individual kinesin constructs can be attributed to different trajectories of aa28, aa215, and aa324 in space, pertaining to the "back," "front," and "middle" part of the head, respectively.

This approach allowed us to reconstruct the 3D orientation of the labeled head in its unbound state. Under the assumption that each kinesin construct entered the 1HB state with its unbound head in between previous and next microtubule-binding sites, the nonapparent displacement of aa215 along the on-axis actually indicates a rotation of the unbound head around its front during a substep. Likewise, the symmetry of substep pairs of construct K28C implies a forward rotation of aa28 by ~8 nm, and the asymmetry of substep pairs of construct T324C suggests a displacement of aa324 by ~6 nm along the microtubule axis when entering the unbound state.

Next, we investigated the off-axis displacement of the unbound head, which has been reported to be rightward (*16*) or nonexistent (*15*) by different bead-tracking studies using an inherently artifact-prone label (*28*). We found off-axis displacements in the unbound state of <2 nm for T324C and up to ~5 nm for K28C (fig. S15). For the entire substep population of K28C, rightward, near-zero, and leftward off-axis displacements appeared. The displacement was always consistent in magnitude and direction within a single trace, as shown by Pearson correlation analysis [ρ = 0.65 ± 0.02 (mean±SD)].

To correlate the observed off-axis displacements with individual protofilament classes of a single microtubule ("sides," "center," and "between") (Fig. 5C), we recorded trace sets (137 traces in total) of construct K28C on 19 different microtubules using actively stabilized samples (for details, see materials and methods section 1.1.3 and fig. S16). The outermost traces of the individual sets were spaced by ~30 nm, which agrees well with the microtubule diameter of ~25 nm (*39*, *40*) plus twice the ~2.5-nm distance between the labeling position of construct K28C and the microtubule surface (inferred from PDB 3J8Y). Thus, these traces were assigned to kinesins walking along side protofilaments and were used as references for the remaining trace assignment.

Located between two side traces, the center traces exhibit pronounced rightward displacement into the unbound state (Fig. 5D). After aligning all trace sets along their central on-axes, the substep off-axis displacements were plotted against the lateral offsets of the corresponding traces from the microtubule center axis (Fig. 5E). Imperfections in the alignment of all trace sets may introduce minor errors in position, but the traces of kinesins walking along side protofilaments display a near-zero off-axis displacement of their unbound states, ruling out a considerable displacement of aa28 away from the microtubule surface. Because protofilaments at the bottom of microtubules were mostly blocked by neutravidin and polymer (Fig. 5C), virtually all of the center traces can be attributed to kinesins walking on the microtubule's top. These traces showed maximum and predominantly rightward off-axis displacements into the unbound state. This finding is corroborated by further detailed analysis of the between traces generated by kinesins walking both on top and bottom protofilaments, leading to both rightward (for top) and leftward (for bottom) off-axis displacements for simple geometric reasons (see supplementary text section 2.7). We conclude that upon entering the unbound intermediate state, aa28 of the trailing head is displaced up to ~5 nm rightward with respect to the kinesin coordinate system.

The combination of on-axis substep sizes and associated off-axis displacements of the investigated amino acid positions allowed us to derive an approximate average 3D orientation of the unbound head during kinesin motion (Fig. 5F and movies S1 and S2), improving and specifying the ones derived from FRET studies (*35*, *38*). In conjunction with stalk rotation (Fig. 3), which is expected to resolve torsion and thus decrease asymmetry caused by a head's full step, our data showing systematic rightward displacement of the unbound head indicate that the hand-over-hand stepping is symmetric.

Our model of the mechanochemical cycle of kinesin (visualized in fig. S17) is based on MINFLUX tracking with 3 nm/0.63 ms STR per individual localization using just 20 detected photons, allowing the identification of >12,000 kinesin steps with 1-nm precision (fig. S18). We believe that this performance sets a benchmark for protein tracking. Fluorophores with higher emission rates will increase the STR even further. The confocal arrangement of the MINFLUX system, because it strongly suppresses background, also allows for protein investigations in living cells (*41*). In fact, one can readily envisage applying MINFLUX to any nanometer-scale changes of fluorescently labeled biomolecules. We thus believe that our study establishes MINFLUX as a next-generation tool for recording conformational changes of single proteins with minimal invasiveness.

REFERENCES AND NOTES

1. K. Svoboda, C. F. Schmidt, B. J. Schnapp, S. M. Block, *Nature* **365**, 721–727 (1993).
2. K. Svoboda, S. M. Block, *Annu. Rev. Biophys. Biomol. Struct.* **23**, 247–285 (1994).
3. M. J. Schnitzer, S. M. Block, *Nature* **388**, 386–390 (1997).
4. Y. Seol, A. E. Carpenter, T. T. Perkins, *Opt. Lett.* **31**, 2429–2431 (2006).
5. A. Yildiz *et al*., *Science* **300**, 2061–2065 (2003).
6. A. Yildiz, M. Tomishige, R. D. Vale, P. R. Selvin, *Science* **303**, 676–678 (2004).
7. R. E. Thompson, D. R. Larson, W. W. Webb, *Biophys. J.* **82**, 2775–2783 (2002).
8. A. R. Dunn, J. A. Spudich, *Nat. Struct. Mol. Biol.* **14**, 246–248 (2007).
9. F. Ruhnow, D. Zwicker, S. Diez, *Biophys. J.* **100**, 2820–2828 (2011).
10. J. Ortega-Arroyo, P. Kukura, *Phys. Chem. Chem. Phys.* **14**, 15625–15636 (2012).
11. E. Reid *et al*., *Am. J. Hum. Genet.* **71**, 1189–1194 (2002).
12. M. Fichera *et al*., *Neurology* **63**, 1108–1110 (2004).
13. K. Poirier *et al*., *Nat. Genet.* **45**, 639–647 (2013).
14. G. Chandrasekaran, P. Tátrai, F. Gergely, *Br. J. Cancer* **113**, 693–698 (2015).
15. K. J. Mickolajczyk *et al*., *Proc. Natl. Acad. Sci. U.S.A.* **112**, E7186–E7193 (2015).
16. H. Isojima, R. Iino, Y. Niitani, H. Noji, M. Tomishige, *Nat. Chem. Biol.* **12**, 290–297 (2016).
17. F. Balzarotti *et al*., *Science* **355**, 606–612 (2017).
18. Y. Eilers, H. Ta, K. C. Gwosch, F. Balzarotti, S. W. Hell, *Proc. Natl. Acad. Sci. U.S.A.* **115**, 6117–6122 (2018).
19. K. C. Gwosch *et al*., *Nat. Methods* **17**, 217–224 (2020).
20. R. Schmidt *et al*., *Nat. Commun.* **12**, 1478 (2021).
21. T. A. Klar, E. Engel, S. W. Hell, *Phys. Rev. E* **64**, 066613 (2001).
22. R. Killick, P. Fearnhead, I. A. Eckley, *J. Am. Stat. Assoc.* **107**, 1590–1598 (2012).
23. H. Kojima, E. Muto, H. Higuchi, T. Yanagida, *Biophys. J.* **73**, 2012–2022 (1997).
24. W. Hua, J. Chung, J. Gelles, *Science* **295**, 844–848 (2002).
25. B. Gutiérrez-Medina, A. N. Fehr, S. M. Block, *Proc. Natl. Acad. Sci. U.S.A.* **106**, 17007–17012 (2009).
26. A. Ramaiya, B. Roy, M. Bugiel, E. Schäffer, *Proc. Natl. Acad. Sci. U.S.A.* **114**, 10894–10899 (2017).
27. S. Sudhakar *et al*., *Science* **371**, eabd9944 (2021).
28. K. J. Mickolajczyk, A. S. I. Cook, J. P. Jevtha, J. Fricks, W. O. Hancock, *Biophys. J.* **117**, 331–345 (2019).
29. S. Hasnain, M. L. Mugnai, D. Thirumalai, *J. Phys. Chem. B* **125**, 10432–10444 (2021).
30. J. Howard, *Annu. Rev. Physiol.* **58**, 703–729 (1996).
31. R. Takaki, M. L. Mugnai, Y. Goldtzvik, D. Thirumalai, *Proc. Natl. Acad. Sci. U.S.A.* **116**, 23091–23099 (2019).
32. W. O. Hancock, *Biophys. J.* **110**, 1216–1225 (2016).

33. J. Qin, H. Zhang, Y. Geng, Q. Ji, *Int. J. Mol. Sci.* **21**, 6977 (2020).
34. E. Mandelkow, K. A. Johnson, *Trends Biochem. Sci.* **23**, 429–433 (1998).
35. S. Verbrugge, Z. Lansky, E. J. Peterman, *Proc. Natl. Acad. Sci. U.S.A.* **106**, 17741–17746 (2009).
36. K. J. Mickolajczyk, W. O. Hancock, *Biophys. J.* **112**, 2615–2623 (2017).
37. A. Toleikis, N. J. Carter, R. A. Cross, *Biophys. J.* **119**, 1984–1994 (2020).
38. T. Mori, R. D. Vale, M. Tomishige, *Nature* **450**, 750–754 (2007).
39. W. Brinkley, *J. Struct. Biol.* **118**, 84–86 (1997).
40. M. C. Ledbetter, K. R. Porter, *Science* **144**, 872–874 (1964).
41. T. Deguchi *et al*., *Science* **379**, 1010–1015 (2023).
42. J. O. Wolff *et al*., Matlab scripts for: MINFLUX dissects the unimpeded walking of kinesin-1, Zenodo (2022); https://doi.org/10.5281/zenodo.7442902.
43. J. O. Wolff, L. Scheiderer, Raw data for: MINFLUX dissects the unimpeded walking of kinesin-1, Zenodo (2022); https://doi.org/10.5281/zenodo.7565676.

ACKNOWLEDGMENTS

We thank M. Tarnawski and the Protein Core Facility at the MPI Heidelberg for performing the QuikChange site-directed mutagenesis and protein expression; our colleague M. Remmel for access to the TIRF microscope; the MS Core Facility at the MPI Heidelberg for recording the mass spectroscopy data; R. Vale (University of California, San Francisco and Howard Hughes Medical Institute) for providing plasmids K560CLM T324C and CLM RP HTR; A. Yildiz (University of California, Berkeley) for providing plasmid K560CLM E215C and the protein preparation and purification protocol; and M. Kulp (Optical Facility, MPI Göttingen) for imprinting aluminum gratings on coverslips. **Author contributions:** J.O.W. and T.E. built the microscope and together with J.E. wrote the software for controlling the setup and performing measurements. J.E. designed the interferometric system with input from S.W.H. and provided technical supervision. J.O.W. built the active stabilization unit, wrote software for MINFLUX track evaluation, and performed measurements initially together with T.E. L.S. scrutinized the kinesin tracking literature, designed the kinesin experiments, and prepared the related samples advised by J.M. L.S. and J.O.W. processed, evaluated, and interpreted kinesin measurements co-supervised by J.M., who was also responsible for the project administration. S.W.H. proposed and initiated the evaluation of MINFLUX spatiotemporal resolution for protein tracking and was responsible for overall supervision and steering. L.S., J.O.W., J.M., and S.W.H. wrote the manuscript with input from all authors. All authors contributed to the results through critical discussions throughout the course of the project. **Competing interests:** S.W.H. is inventor on patent applications WO 2013/072273 and WO 2015/097000 submitted by the Max Planck Society that cover basic principles and arrangements of MINFLUX, including single-molecule tracking. J.E. and S.W.H. are inventors on patent application WO 2020/064108 submitted by the Max Planck Society that covers principles and arrangements of the phase/amplitude modulator for shifting the intensity minimum. S.W.H. is a cofounder of the company Abberior Instruments, which commercializes MINFLUX microscopes. The remaining authors declare no competing interests. **Funding:** This work was funded by intramural funds from the Max Planck Society. **Code and data availability:** Matlab scripts used for the sliding-curvature and fixed-curvature estimator, as well as the step-finder and the hidden Markov model and DNA sequences, have been deposited at Zenodo (*42*). Raw data and Matlab scripts for displaying and processing the data can be downloaded from Zenodo (*43*).

SUPPLEMENTARY MATERIALS

science.org/doi/10.1126/science.ade2650
Materials and Methods
Supplementary Text
Figs. S1 to S20
Tables S1 to S4
References (*44*–*47*)
Movies S1 and S2
MDAR Reproducibility Checklist

View/request a protocol for this paper from *Bio-protocol*.

Submitted 4 August 2022; accepted 23 January 2023
10.1126/science.ade2650

MINFLUX dissects the unimpeded walking of kinesin-1

Jan O. Wolff, Lukas Scheiderer, Tobias Engelhardt, Johann Engelhardt, Jessica Matthias, and Stefan W. Hell

Science **379** (6636), . DOI: 10.1126/science.ade2650

Zeroing in on motor proteins

The super-resolution microscopy technique MINFLUX enables localization of fluorophores using a minimal number of photons. Two studies now expand on the development and implementation of MINFLUX to track motor protein dynamics in vitro and in cells (see the Perspective by Fei and Zhou). Wolff *et al*. refined the precision of MINFLUX such that single-fluorophore tracking with nanometer precision was possible with only tens of photons. They tracked the movement of kinesin-1 on microtubules and were able to see individual 4-nanometer substeps and rotation of the protein during stepping in their analysis. Deguchi *et al*. applied MINFLUX with a labeling and tracking approach called motor-PAINT to monitor stepping of motor proteins on microtubules in living and fixed cells in both two and three dimensions. —MAF

Science (ISSN 1095-9203) is published by the American Association for the Advancement of Science. 1200 New York Avenue NW, Washington, DC 20005. The title *Science* is a registered trademark of AAAS.